



CHORUS

This is the accepted manuscript made available via CHORUS. The article has been published as:

Asymmetric rectified electric fields between parallel electrodes: Numerical and scaling analyses

S. M. H. Hashemi Amrei, Gregory H. Miller, and William D. Ristenpart

Phys. Rev. E **99**, 062603 — Published 10 June 2019

DOI: [10.1103/PhysRevE.99.062603](https://doi.org/10.1103/PhysRevE.99.062603)

Asymmetric Rectified Electric Fields between Parallel Electrodes: Numerical and Scaling Analyses

S. M. H. Hashemi Amrei, Gregory Miller,* and William D. Ristenpart†

Department of Chemical Engineering, University of California Davis, Davis, California 95616, United States

(Dated: May 26, 2019)

Recent computational and experimental work has established the existence of Asymmetric Rectified Electric Fields (AREFs), a type of steady electric field that occurs in liquids in response to an applied oscillatory potential, provided the ions present have different mobilities [Hashemi Amrei *et al.*, Phys. Rev. Lett. **121**, 185504, 2018]. Here we use scaling analyses and numerical calculations to elaborate the nature of one-dimensional AREFs between parallel electrodes. The AREF magnitude is shown to increase quadratically with applied potential at low potentials, increase nonlinearly at intermediate potentials, then increase with a constant rate slower than quadratically at sufficiently high potentials, with no impact at any potential on the spatial structure of the AREF. In contrast, the AREF peak location increases linearly with a frequency-dependent diffusive length scale for all conditions tested, with corresponding decreases in both the magnitude and number of sign changes in the directionality of AREF. Furthermore, both the magnitude and spatial structure of the AREF depend sensitively on the ionic mobilities, valencies, and concentrations, with a potential-dependent peak AREF magnitude occurring at an ionic mobility ratio of $D_-/D_+ \lesssim 5$. The results are summarized with approximate scaling expressions that will facilitate interpretation of the steady component for oscillatory fields in liquid systems.

I. INTRODUCTION

The application of an oscillatory electric potential to a liquid is an integral aspect of a wide range of phenomena, including AC electroosmosis (ACEO) pumps [1–4], induced charge electrokinetics (ICEK) [5–14], electrohydrodynamic (EHD) manipulation of colloids [15–20] and bioparticles [21–24], dielectric and impedance spectroscopy [25–28], cyclic voltammetry [29–31], electro-acoustics [32–34], dielectrophoresis [35–39], and electroosmotic electrolyte transport through charged nanopores/nanotubes [40, 41]. In all of these systems, interpretation of the experimental observations depends on information regarding the dynamic response of the liquid to the applied potential. In particular, a key question is the nature inside the liquid of the electric field itself, which is not directly measurable and thus must be calculated theoretically. Traditionally, the “standard electrokinetic model,” which couples the Poisson equation with Nernst-Planck ion transport equations, has served as the starting point for analysis of liquids with dissociated ions [42]. Because the governing equations are coupled and highly nonlinear, and because under typical conditions large disparities in length and time scales render the equations extremely stiff, most analyses of the electric field have focused on asymptotically small applied potentials [25, 43–46] or on higher applied potentials but for ions with equal mobilities [47–49].

Despite being widely used, however, these linearized and equal-mobility models have yielded predictions at odds with experimental observations in a variety of systems. For example, researchers investigating ACEO

pumps have long been stymied by the observed reversal of fluid flow direction upon varying the applied frequency [4, 12, 13]. Likewise, in work examining the EHD aggregation of colloids near electrodes, the effect of electrolyte type on the aggregation behavior has remained mysterious despite numerous theoretical and experimental studies [50–54]. Recent experimental studies revealed that colloidal particles can levitate several particle diameters upward against gravity in response to an oscillatory field, provided they were suspended in certain electrolytes (e.g., NaOH and KOH) [55, 56], a result also inexplicable in terms of the traditional solutions to the standard electrokinetic model.

Recent work by Hashemi Amrei *et al.* [57] generated a new possible explanation for the above unresolved questions. Specifically, they showed that application of a perfectly sinusoidal potential to a liquid counterintuitively yields a long-range steady electric field. This steady field results from the asymmetry in motion of the positive and negative ions as they move back and forth in the oscillatory field, a phenomenon explicable even in the limit of just two isolated ions (Fig. 1). Denoted as an Asymmetric Rectified Electric Field (AREF), the magnitude of the steady field depends on the ratio $\delta = D_-/D_+$ of the relative diffusivities of the ions. We emphasize that AREF is necessarily a *nonlinear* effect; any sort of linearization results in a zero time average solution. Numerical solutions to the full nonlinear electrokinetic model further corroborated the existence of AREF [57]. The numerical results show that AREFs persist over large length scales between parallel electrodes, with a characteristic diffusive length scale given by $\ell_D \sim \sqrt{D/f}$, where D is a characteristic diffusivity and f is the applied frequency (Fig. 2). These predictions were shown to be consistent with the levitation behavior of colloids to extreme distances away from the electrode; the long range steady field lifts par-

* Email: grgmiller@ucdavis.edu

† Email: wdristenpart@ucdavis.edu

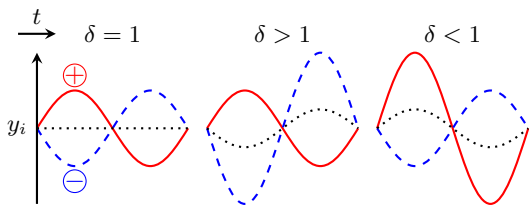


FIG. 1. Illustration of two-ion model: harmonic oscillations ($y_i(t)$) of two oppositely charged isolated ions in response to a sinusoidal electric field for different $\delta = D_-/D_+$ values. The generated electric field at an arbitrary location $y = y_f$ due to these harmonic oscillations is asymmetrical and has a nonzero time average for $\delta \neq 1$. The dotted black curves denote the oscillations of the center of charge.

ticles electrophoretically upward until the AREF diminishes sufficiently to balance gravity [57, 58]. As discussed by Hashemi Amrei et al., the existence of AREFs also potentially explains the unresolved frequency and electrolyte dependencies observed in ACEO pumps and EHD aggregation of particles near electrodes [57].

Several fundamental questions about AREFs, however, to date remain unanswered. Notably, the scaling of the AREF with the magnitude of the applied potential was only elucidated for small potentials, and it is unclear how AREFs scale with larger applied potentials. It is also unclear how the spatial structure of the AREF varies with frequency (and the corresponding diffusive length scale ℓ_D), an important question since the earlier results indicated that even the sign of the AREF (i.e., the direction of the steady field) changes repeatedly as a function of frequency. Likewise, although a non-unity diffusivity ratio ($\delta \neq 1$) is clearly necessary for an AREF to occur, it is unclear how the magnitude and the spatial structure (shape) of the AREF scale with δ or with the valencies of the ions themselves.

In this work, we address the above questions by elaborating the nature of one-dimensional AREFs between parallel electrodes. We perform a systematic dimensional analysis and extensive numerical calculations over a large parameter space, focusing on the limit of negligible electrochemical and thermal effects. The analysis yields several key results:

Potential: The AREF magnitude increases quadratically with applied potential at low potentials, increases nonlinearly at intermediate potentials, and increases slower than quadratically at sufficiently high potentials. The applied potential does not affect the AREF shape.

Frequency: The AREF peak location far from the electrode is linearly proportional to $\ell_D = \sqrt{D/f}$ for all conditions tested, but the magnitude decreases with a power-law exponent ranging between ℓ_D^{-1} and ℓ_D^{-3} depending on the applied potential. As ℓ_D decreases (f increases), a series of pitchfork bifurcations occur for the number of zeros in the AREF (i.e., the number of sign changes increases.)

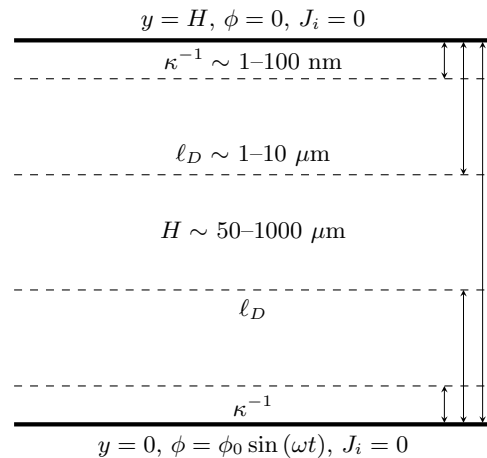


FIG. 2. Schematic diagram of two parallel electrodes and not to scale comparison of different length scales. AREF varies over a diffusive length scale of $\ell_D = \sqrt{D/f}$ which is several orders of magnitude higher than the characteristic length scale of the Debye layer (κ^{-1}).

Ionic strength: The AREF magnitude peaks at ion concentrations (c_∞) similar to those of deionized water, varying as c_∞^{-1} and $c_\infty^{-1/4}$ at low and high applied voltages, respectively.

Ionic mobilities: The AREF magnitude increases with δ to a peak value near $\delta \lesssim 5$, then decays asymptotically back toward zero. The ion valencies dramatically alter the magnitude and sign of the AREF.

Each of the above points is elucidated in detail below. We begin with a formal dimensional analysis, and we demonstrate that under typical circumstances the system behavior is governed by four key dimensionless groups. We then present systematic numerical calculations versus those four parameters to corroborate the above list of key results. Because the numerical calculations are non-trivial, we finish by summarizing the results in terms of approximate scaling expressions that should assist researchers in interpretation of AREF effects in oscillatory fields.

II. THEORY AND NUMERICAL METHODS

A. Standard Electrokinetic Model

Our starting point is the standard electrokinetic model [43, 57, 59], which is a continuum-level model that couples the electric field to the flux of dissociated ions. We restrict attention to fully dissociated binary electrolytes between parallel electrodes located at $y = 0$ and $y = H$ (cf. Fig. 2). The electric potential is governed by the Poisson equation

$$-\varepsilon \frac{\partial^2 \phi}{\partial y^2} = \rho = e(z_+ n_+ + z_- n_-), \quad (1)$$

relating the free charge density to the gradient of the electric field. The transport of ions in space is governed by the Nernst-Planck equations for each ion,

$$\frac{\partial n_i}{\partial t} = D_i \frac{\partial^2 n_i}{\partial y^2} + e z_i \frac{D_i}{k_B T} \frac{\partial}{\partial y} \left(n_i \frac{\partial \phi}{\partial y} \right). \quad (2)$$

Here the symbols stand for applied potential, ϕ_0 ; free charge density, ρ ; elementary charge, e ; charge number, z_i ; permittivity, ε ; electric potential, ϕ ; number concentration of ion, n_i ; diffusivity, D_i ; Boltzmann constant, k_B ; and absolute temperature, T .

The first and second terms on the right hand side of the Nernst-Planck equation (Eq. 2) are the diffusive and electromigrative contributions of the ion transport, respectively. It is the electromigration term that accounts for the transport of ions in direct response to the electric field and is responsible for the nonlinearity of the governing equations. We assume that the liquid is quiescent with no convection due to instabilities or flows generated around suspended objects.

To close the problem, we first subject the potential distribution to the following initial and boundary conditions:

$$\phi(0, y) = 0, \quad (3)$$

$$\phi(t, 0) = \phi_0 \sin(\omega t), \quad \phi(t, H) = 0. \quad (4)$$

At time equal to zero ($t = 0$) a sinusoidal electric potential of amplitude ϕ_0 and angular frequency $\omega = 2\pi f$ is applied on the lower electrode at $y = 0$, while the upper electrode at $y = H$ is kept grounded (Fig. 2).

The ions are initially evenly distributed between the two electrodes with number concentrations of n_i^∞ ,

$$n_i(0, y) = n_i^\infty. \quad (5)$$

The initial ion concentrations are related to the bulk concentration of the electrolyte (n^∞) through their respective charge numbers:

$$n_+^\infty = -z_- n^\infty, \quad n_-^\infty = z_+ n^\infty, \quad (6)$$

which satisfy the electroneutrality condition, $z_+ n_+^\infty + z_- n_-^\infty = 0$.

Finally, we assume that the electrodes are fully ‘blocking,’ such that the flux J_i of both ions through the electrodes is zero,

$$J_i = -D_i \left(\frac{\partial n_i}{\partial y} + \frac{e z_i n_i}{k_B T} \frac{\partial \phi}{\partial y} \right)_{y=0, H} = 0. \quad (7)$$

This assumption might not be justified at high applied voltages and sufficiently low frequencies. Similarly, we neglect any complications due to the formation of a compact Stern layer at the electrodes; some results indicate that a significant potential drop might occur across the Stern layer [47, 60]. We focus here on the limiting case of negligible Stern layer effects and negligible electrochemistry to provide a reference point for future work examining those more complicated physics.

TABLE I. Quantities and dimensions in MLTQ system. M: mass, L: length, T: time, Q: charge. Notation \doteq indicates dimensional equality.

quantity	definition	dimension
z_+	charge number of + ion	dimensionless
z_-	charge number of - ion	dimensionless
ε	permittivity	F/m \doteq M ⁻¹ L ⁻³ T ² Q ²
$k_B T$	thermal energy	N.m \doteq ML ² T ⁻²
e	elementary charge	C \doteq Q
H	electrode spacing	m \doteq L
f	applied frequency	1/s \doteq T ⁻¹
D_+	diffusivity of + ion	m ² /s \doteq L ² T ⁻¹
D_-	diffusivity of - ion	m ² /s \doteq L ² T ⁻¹
ϕ_0	applied electric potential	V \doteq ML ² T ⁻² Q ⁻¹
n^∞	bulk concentration of electrolyte	1/m ³ \doteq L ⁻³
ϕ	electric potential	V \doteq ML ² T ⁻² Q ⁻¹
n_+	concentration of + ion	1/m ³ \doteq L ⁻³
n_-	concentration of - ion	1/m ³ \doteq L ⁻³
y	location	m \doteq L
t	time	s \doteq T

B. Dimensionless Form

The important parameters and variables in our model and their corresponding dimensions are listed in Table I. There are a total of $r = 16$ quantities and $k = 4$ independent dimensions, so by Buckingham’s pi theorem there are $r - k = 12$ dimensionless groups. We choose H , f , $k_B T$, and e as the repeating quantities to define the dimensionless groups.

We use the gap size H and the inverse frequency $1/f$ to scale the independent spatial and temporal variables respectively as

$$\tilde{y} = y/H, \quad \tilde{t} = ft = \omega t / (2\pi). \quad (8)$$

The thermal potential $\phi_T = k_B T/e$ is used to nondimensionalize the applied potential ϕ_0 ,

$$\Phi_0 = \frac{\phi_0 e}{k_B T}, \quad (9)$$

while the applied potential scales the dependent potential $\phi(t, y)$ as

$$\tilde{\phi} = \phi/\phi_0. \quad (10)$$

Note that unlike the traditional linearized case for which ϕ_T is an appropriate characteristic potential, for this non-linear problem ϕ can be as high as $\sim 100\phi_T$. Hence, the applied potential ϕ_0 offers a better normalization of the potential distribution. In addition, the ion concentrations are scaled as

$$\tilde{n}_+ = n_+/n_0, \quad \tilde{n}_- = n_-/n_0, \quad (11)$$

where n_0 is given by

$$n_0 = z_+^2 n_+^\infty + z_-^2 n_-^\infty. \quad (12)$$

Our numerical results (cf. Sec. III C) suggest the characteristic diffusivity of the problem to be

$$\hat{D} = \sqrt{D_+ D_-}, \quad (13)$$

which is used to define the dimensionless diffusive length scale

$$\mathcal{L}_D = \ell_D/H = \frac{\sqrt{\hat{D}/f}}{H}. \quad (14)$$

The ionic mobility mismatch is denoted by the dimensionless parameter

$$\delta = D_-/D_+. \quad (15)$$

Finally, the ionic strength appears in two dimensionless groups, a dimensionless Debye length scale,

$$\kappa H = \sqrt{\frac{n_0 e^2}{\varepsilon k_B T}} H, \quad (16)$$

and an overall dimensionless number concentration,

$$N_\infty = n_0 H^3. \quad (17)$$

The dimensionless groups and variables are summarized in Table II. If we narrow our focus to cases of aqueous electrolytes at ambient temperature (i.e., if we omit situations where thermal effects are important), then the

TABLE II. Dimensionless groups (parameters Π_1 – Π_7) plus dependent and independent variables (Π_8 – Π_{12}). $n_0 = z_+^2 n_+^\infty + z_-^2 n_-^\infty = n^\infty (z_-^2 z_+ - z_+^2 z_-)$, $\kappa^{-1} = \sqrt{\varepsilon k_B T / (n_0 e^2)}$, $\hat{D} = \sqrt{D_+ D_-}$.

Π_1	$\Phi_0 = \phi_0 e / (k_B T)$	Π_2	$\mathcal{L}_D = \ell_D / H = \sqrt{\hat{D} / f} / H$
Π_3	$\delta = D_- / D_+$	Π_4	κH
Π_5	z_+	Π_6	z_-
Π_7	$N^\infty = n_0 H^3$	Π_8	$\tilde{\phi} = \phi / \phi_0$
Π_9	$\tilde{n}_+ = n_+ / n_0$	Π_{10}	$\tilde{n}_- = n_- / n_0$
Π_{11}	$\tilde{t} = ft$	Π_{12}	$\tilde{y} = y / H$

dimensionless groups κH and $n_0 H^3$ become dependent since the only varying quantities in both groups are n_0 and H . Therefore, only one of them (κH) is taken here as a controlling dimensionless group. In other words, the six dimensionless parameters Φ_0 , \mathcal{L}_D , δ , κH , and charge numbers z_+ and z_- completely govern the system behavior.

Using the above definitions, the dimensionless governing equations are written as

$$-\frac{\Phi_0}{(\kappa H)^2} \frac{\partial^2 \tilde{\phi}}{\partial \tilde{y}^2} = z_+ \tilde{n}_+ + z_- \tilde{n}_-, \quad (18)$$

$$\frac{\partial \tilde{n}_+}{\partial \tilde{t}} = \frac{\mathcal{L}_D^2}{\sqrt{\delta}} \left[\frac{\partial^2 \tilde{n}_+}{\partial \tilde{y}^2} + z_+ \Phi_0 \frac{\partial}{\partial \tilde{y}} \left(\tilde{n}_+ \frac{\partial \tilde{\phi}}{\partial \tilde{y}} \right) \right], \quad (19)$$

$$\frac{\partial \tilde{n}_-}{\partial \tilde{t}} = \sqrt{\delta} \mathcal{L}_D^2 \left[\frac{\partial^2 \tilde{n}_-}{\partial \tilde{y}^2} + z_- \Phi_0 \frac{\partial}{\partial \tilde{y}} \left(\tilde{n}_- \frac{\partial \tilde{\phi}}{\partial \tilde{y}} \right) \right], \quad (20)$$

subject to the following dimensionless initial conditions,

$$\tilde{n}_i(0, \tilde{y}) = n_i^\infty / n_0, \quad (21a)$$

$$\tilde{\phi}(0, \tilde{y}) = 0, \quad (21b)$$

and dimensionless boundary conditions,

$$\left(\frac{\partial \tilde{n}_i}{\partial \tilde{y}} + z_i \Phi_0 \tilde{n}_i \frac{\partial \tilde{\phi}}{\partial \tilde{y}} \right)_{\tilde{y}=0,1} = 0, \quad (22a)$$

$$\tilde{\phi}(\tilde{t}, 0) = \sin(2\pi\tilde{t}), \quad \tilde{\phi}(\tilde{t}, 1) = 0. \quad (22b)$$

In Eq. 21a, the dimensionless initial ion concentrations can be written in terms of charge numbers (z_+ & z_-):

$$\frac{n_+^\infty}{n_0} = \frac{-z_-}{z_-^2 z_+ - z_+^2 z_-}, \quad \frac{n_-^\infty}{n_0} = \frac{z_+}{z_-^2 z_+ - z_+^2 z_-}. \quad (23)$$

Finally, using the above scalings, all forms of the electric field $E = -\partial\phi/\partial y$, including the instantaneous and time average, become nondimensionalized by the nominal electric field ϕ_0/H ,

$$\tilde{E} = EH/\phi_0. \quad (24)$$

The time average electric field is obtained by time integration over one AC cycle of the harmonic solution as

$$\langle \tilde{E} \rangle = \int_0^1 \tilde{E} d\tilde{t}. \quad (25)$$

Likewise, the dimensionless free charge density becomes

$$\tilde{\rho} = \rho/n_0 = (z_+ n_+ + z_- n_-)/n_0, \quad (26)$$

with its time average denoted by $\langle \tilde{\rho} \rangle$.

C. Numerical Solution

Following the procedure outlined by Hashemi Amrei et al. [57], the system of nonlinear partial differential equations (Eqs. 18–22) was numerically solved using multigrid finite difference methods [61, 62] and mesh refinement [63]. Cell-centered finite difference methods were employed to discretize the governing equations and boundary conditions. A typical minimum cell size used for the simulations is of order $\kappa^{-1}/128$ which, for $\kappa^{-1} \approx 13$ nm, is equivalent to ≈ 0.1 nm. Such a small size step (compared to electrodes spacing which can be several hundred microns) restricts the time marching of the simulation. In the presence of convective terms (with a velocity of u), the Courant-Friedrichs-Lewy (CFL) number condition limits the maximum allowable time step of the numerical solution: $|u|\Delta t/h \leq 1$, with Δt and h as the temporal and spatial steps. In dimensional context, the electromigration term of the species continuity equation (Eq. 2) can be written as $\frac{\partial}{\partial y}(un_i)$ with $u = \frac{ez_i D_i}{k_B T} \frac{\partial \phi}{\partial y}$ ($[u] = \text{m/s}$), resembling a convective transport of ions. Therefore, we require

$$\left| \frac{ez_i D_i}{k_B T} \frac{\partial \phi}{\partial y} \right| \Delta t/h \leq 1. \quad (27)$$

It is not practical to cover the entire domain with a uniform cell size that is small enough to resolve the Debye layer (e.g., covering 100 μm with $h \approx 0.1$ nm requires 1 million cells). Therefore, we used mesh refinement near the electrode surfaces [63].

Operator splitting is employed. For each time step, the Poisson equation (Eq. 18) is solved for Φ_0 (step i), which is subsequently used to find the ion concentrations from the Nernst-Planck equations (Eqs. 19 & 20) (step ii). Our Poisson solver is based on the algorithm of Martin and Cartwright [63]. With some changes, a similar algorithm is devised to solve the species continuity equation. The main difference of the algorithm is the inclusion of the nonlinear electromigration term. To ensure solution stability, the CFL number is calculated prior to step ii. While the condition is not met, we set $\Delta t = \Delta t/2$ to find a $\Delta t = (\Delta t)_c$ that satisfies the condition. Then step ii breaks down into $\Delta t/(\Delta t)_c$ substeps.

Besides the above-mentioned challenges, achieving a harmonic solution by solving the dynamical equations is computationally intensive [47]. The simulation time t_f should be long enough for the ions to transfer back and forth between the electrodes in order to reach the **harmonic solution**. The ions transfer with diffusive and electromigrative mechanisms with corresponding time scales of $\tau_i^D = H^2/D_i$ and $\tau_i^e = \tau_i^D/(|z_i|\phi_0 e/(k_B T))$. Therefore, to ensure the **harmonic** conditions we require $t_f \gg \max[\tau_i^D, \tau_i^e]$. The time scale of the applied potential is also $\tau^{AC} = 1/f$ which is, for the range of parameters used in this study, far less than τ_i^D and τ_i^e . Therefore, the number of AC cycles should be $n_{AC} \gg \max[\tau_i^D, \tau_i^e]/\tau^{AC}$.

We performed several consistency checks. In this regard, an important issue to consider was the crowding ef-

fect [64]. The finite size of ions enforces a cutoff number concentration of $n_{\text{max}} = 1/l^3$, where l is a characteristic length of the dissolved ions ($n_{\text{max}} \approx 60$ M for $l = 0.3$ nm). We never observed concentrations higher than the maximum packing value. As another consistency check, the instantaneous electric field at the electrode surface was compared to the typical Debye layer field strength κH . Similarly, the maximum instantaneous induced zeta potential ζ on the electrode surface was of the same order of magnitude as the applied potential (i.e., $\zeta \sim \phi_0$). In other words, all of the potentials, field strengths, and ion concentrations are physical. Please see the supplemental material in Hashemi Amrei et al. [57] for further details.

III. NUMERICAL RESULTS

In this section, we systematically investigate the effect of the different system properties on the AREF. **The results are provided at ambient temperature for 1-1 aqueous electrolytes, unless otherwise stated (cf. Sec. III F).** We first analyze univalent electrolytes ($z_+ = |z_-| = 1$), so that the contributing dimensionless parameters are Φ_0 (dimensionless applied potential), \mathcal{L}_D (dimensionless diffusive length scale), δ (ionic mobility mismatch), and κH (dimensionless Debye parameter). Then we discuss the complications that charge numbers (z_+ , z_-) and their potential asymmetry bear to the analysis.

A. Representative field and charge distributions

Figure 3 shows representative time variations of the instantaneous electric field \tilde{E} and free charge density $\tilde{\rho}$ for two different values of \mathcal{L}_D and different Φ_0 values. At low applied potentials, the system behaves linearly and a single-mode sinusoidal solution is obtained ($\Phi_0 = 1$, dotted red curves), consistent with linearized asymptotic analyses [25, 46]. As the applied potential increases, the nonlinear contribution gradually dominates, yielding multimodal solutions. This behavior is in marked contrast to that of linearized solutions, where regardless of the applied potential the solution is invariably a sinusoid. A comparison between the cases of different \mathcal{L}_D values reveals an increase in the amplitude of the harmonic solutions for smaller dimensionless diffusive length scales. For instance, increasing the applied frequency, which results in lower values of \mathcal{L}_D , increases the AREF amplitude. The shape of the harmonics is also affected by \mathcal{L}_D , i.e., the curves for different \mathcal{L}_D values do not collapse.

In this example the ionic mobility mismatch is held constant at $\delta = 3$; hence the time averages are nonzero and a net steady field ($\langle \tilde{E} \rangle$, AREF hereafter) exists within the liquid [57], as shown in Fig. 4(a). The corresponding time average of the free charge density ($\langle \tilde{\rho} \rangle$) is provided in Fig. 4(b). Interestingly, the spatial distributions of AREF and $\langle \tilde{\rho} \rangle$ are, respectively, anti-symmetrical and symmetrical with respect to the midplane as a con-

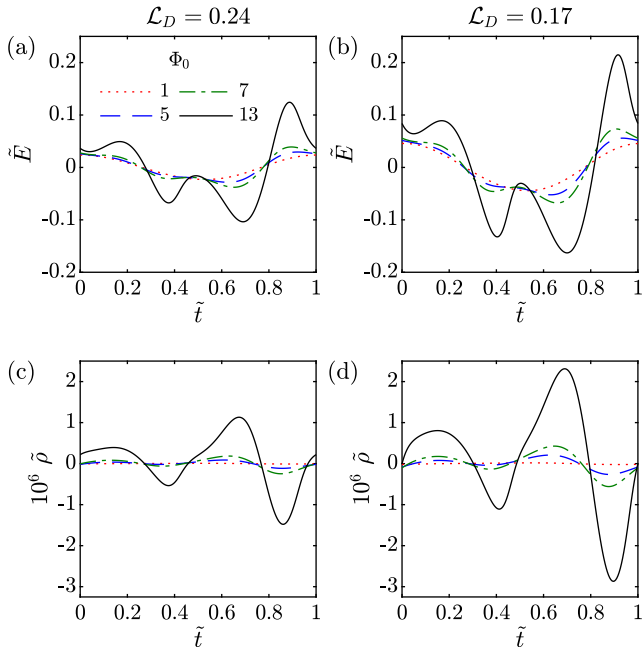


FIG. 3. Representative time variations of the electric field (\tilde{E}) (a & b) and free charge density ($\tilde{\rho}$) (c & d) at $\tilde{y} = 0.04$ for different values of Φ_0 and \mathcal{L}_D . For all plots, $\delta = 3$, $\kappa H = 2600$.

sequence of the mathematical structure of the governing equations. We emphasize that swapping the grounded and powered electrodes does not change the sign or magnitude of $\langle \tilde{E} \rangle$ or $\langle \tilde{\rho} \rangle$; the symmetry of the system is broken by the ionic mobility mismatch, not the relative orientation of the electrodes. The magnitudes of both the time averages of electric field and free charge density increase with the applied potential. Note that wherever the gradient of AREF is zero, there is likewise a zero time average free charge density, consistent with Gauss's law (Eq. 1). In addition, the general shape of the AREF distribution is the same for different applied voltages. In other words, the curves for different Φ_0 values in Fig. 4(a) collapse under appropriate scaling, although as discussed below, the appropriate scaling is non-obvious.

Magnification of the AREF and $\langle \tilde{\rho} \rangle$ distributions near the electrode, on the Debye length scale, are shown in Figs. 4(c) and (d), respectively. The electric field starts from a nonzero value (indiscernible at this scale) at the electrode ($\tilde{y} = 0$), then rises to an absolute maximum before decaying to the solution at the micron scale shown in Fig. 4(a). The free charge density has an absolute nonzero value near the electrode (negative in this representative example), consistent with the nonzero gradient of the AREF at $\tilde{y} = 0$ based on Gauss's law. The mismatch in ionic mobilities yields a net accumulation of ions near the electrodes which subsequently results in AREF.

We focus throughout this section on the AREF behavior at the micron scale, far outside of the Debye layer immediately next to the electrode, since it is in this regime where a steady field will most readily induce experimen-

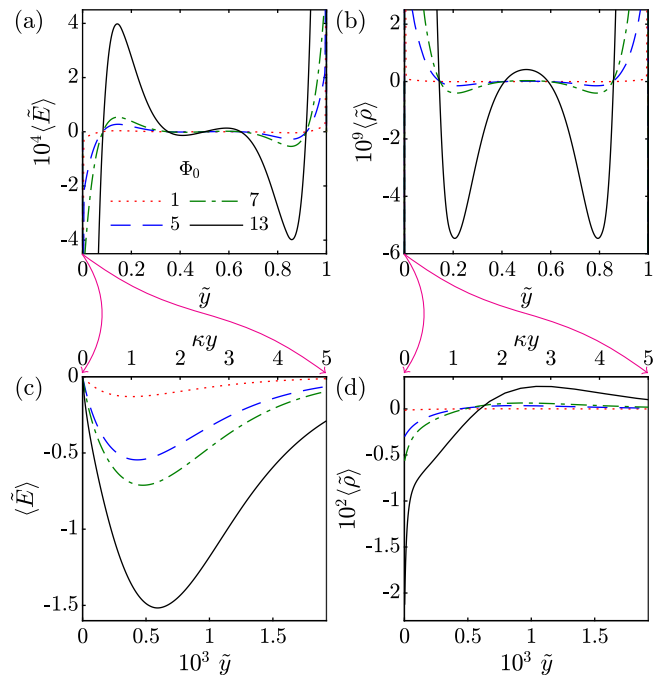


FIG. 4. Representative spatial distribution of AREF ($\langle \tilde{E} \rangle$) and time average free charge density ($\langle \tilde{\rho} \rangle$) at micron scale (a & b) and close to the electrode surface (c & d) for different values of Φ_0 . For all plots, $\mathcal{L}_D = 0.17$, $\delta = 3$, $\kappa H = 2600$.

tally observable behavior with micron scale or larger objects.

B. Effect of applied potential (Φ_0)

To further analyze the effect of applied potential, consider an illustrative example of an AREF distribution depicted in Fig. 5(a). We denote the first peak of AREF outside the Debye layer as $\langle \tilde{E} \rangle_{\text{peak}}$, and \tilde{y}_{peak} is the corresponding dimensionless location of the peak. As discussed in Fig. 4(a), the general shape of the AREF distribution is insensitive to the applied voltage; as a result, the peak location of AREF remains the same at different Φ_0 values. The peak magnitude however is significantly affected by Φ_0 . Figure 5(b) shows $\langle \tilde{E} \rangle_{\text{peak}}$ versus Φ_0 for different values of \mathcal{L}_D . Regardless of \mathcal{L}_D , at low voltages ($\Phi_0 < 1$), $\langle \tilde{E} \rangle_{\text{peak}}$ increases as the first power of Φ_0 . Recall that the electric field is scaled by ϕ_0/H ; hence, the dimensional AREF accordingly varies as ϕ_0^2 . At higher Φ_0 values, the behavior becomes more intricate. The power-law exponent a (local slope of the curves) initially increases due to the contribution of nonlinear terms. However, upon further increasing Φ_0 , a starts dropping to reach a final constant, the value of which depends on the other dimensionless parameters. A representative example of this behavior is demonstrated in Fig. 5(c) for $\mathcal{L}_D = 0.24$. By increasing Φ_0 , the power-law exponent a dramatically ascends from 1 and then drops to a con-

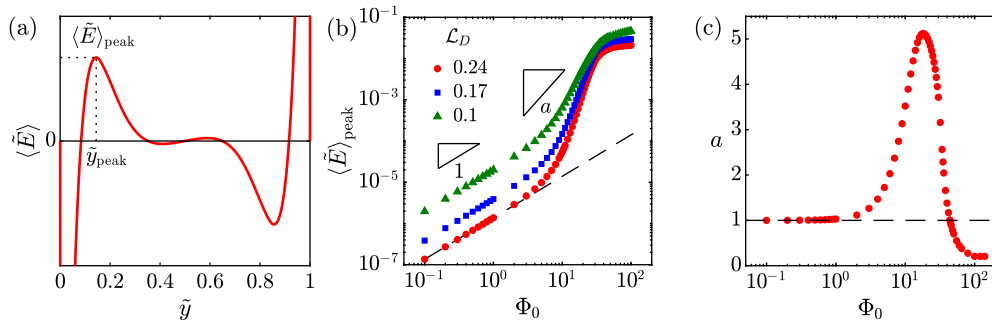


FIG. 5. (a) Illustrative example of AREF distribution with its peak magnitude ($\langle \tilde{E} \rangle_{\text{peak}}$) and the corresponding peak location (\tilde{y}_{peak}) for $\delta > 1$. (b) AREF peak magnitude versus Φ_0 for different values of \mathcal{L}_D . (c) Effect of Φ_0 on the power-law exponent a ($\mathcal{L}_D = 0.24$). For all plots, $\delta = 3$, $\kappa H = 2600$.

stant value below 1. Qualitatively similar results were obtained for different δ and κH values, but the exact dependence of the power a on the applied voltage and other controlling parameters is unclear. Overall, we could not find a universal scaling argument at intermediate/high applied voltages (cf. Sec. IV).

Although the exact mathematical scaling is complicated, the overall physical picture is clear: higher applied oscillatory potentials invariably yield a higher steady field in the bulk. Any physical phenomena directly proportional to the magnitude of the AREF, such as instantaneous electrophoretic velocities, will likewise increase with the applied potential, following dependencies similar to those plotted in Fig. 5(b). Importantly, however, increases in the applied potential have no effect on the spatial structure of the steady AREF. This aspect has a key physical implication: any experimental observables that depend on the zeros in the AREF, such as the equilibrium heights of particles moving electrophoretically in response to the AREF, will be independent of the applied potential. Indeed, such behavior is observed experimentally with colloids balancing between gravity and electrophoresis [58].

C. Effect of diffusive length scale (\mathcal{L}_D)

The second key dimensionless parameter is \mathcal{L}_D , the frequency-dependent diffusive length scale. Figure 6(a) shows the effect of the dimensionless diffusive length scale \mathcal{L}_D on the spatial distribution of AREF. In contrast to Φ_0 , which had no impact on the spatial structure of the AREF, \mathcal{L}_D has a tremendous impact on the shape of the AREF. By increasing the \mathcal{L}_D value, the AREF shifts away from the electrode surface and its peak value decreases (Fig. 6(a)). At higher \mathcal{L}_D values the ions move longer distances during each AC cycle; therefore, the nonlinear effects extend farther away from the electrode surface, with the AREF peak location shifting toward the midplane. Quantitative analysis of the peak location \tilde{y}_{peak} reveals that it is linearly proportional to \mathcal{L}_D

(Fig. 6(b)). The AREF peaks at the same location for different voltages, consistent with the results presented in Fig. 4(a), where the general shape of AREF is conserved regardless of the applied potential. Further increasing the dimensionless diffusive length scale beyond the case of $\mathcal{L}_D = 0.37$ (Fig. 6(a), dotted red curve) eventually results in a curve with no peak outside the Debye layer. To be more precise, for a peak to exist, we require $\mathcal{L}_D < 1/2 \rightarrow \ell_D < H/2$, i.e., the diffusive length scale should not be larger than half of the domain size. Otherwise, the antisymmetric nature of AREF rules out the existence of a peak.

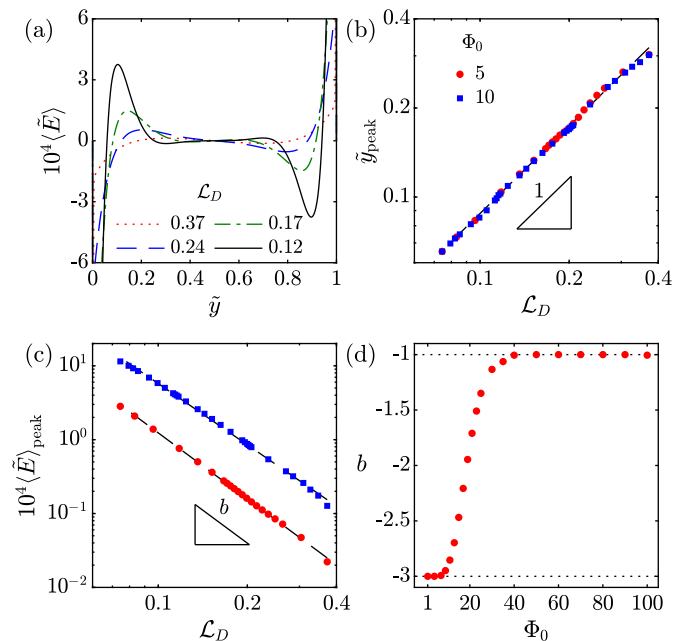


FIG. 6. Effect of \mathcal{L}_D on AREF behavior. (a) Spatial distribution of AREF for different \mathcal{L}_D values ($\Phi_0 = 10$). (b) Peak location of AREF (\tilde{y}_{peak}) versus \mathcal{L}_D . (c) Peak magnitude of AREF ($\langle \tilde{E} \rangle_{\text{peak}}$) versus \mathcal{L}_D . (d) Effect of Φ_0 on the power-law exponent b . For all plots, $\delta = 3$, $\kappa H = 2600$.

The peak magnitude of AREF is also plotted versus \mathcal{L}_D in Fig. 6(c). The general trend is descending. This observation can be understood considering a case where the ions move much faster than the AC time scale (i.e., $\mathcal{L}_D \gg 1$). Under such conditions, on changing the applied potential with the time scale $1/f$, ions have enough time to spatially transfer and screen out any changes in the potential distribution. It is feasible to argue that for AREF to occur, the ions should only partially screen the applied potential. In other words, the ions should fall behind the AC potential in oscillation. Therefore at very high \mathcal{L}_D values AREF is expected to eventually descend to zero. The power-law exponent b of this descending trend, however, is a function of the applied voltage (Fig. 6(d)). The power-law exponent of the AREF magnitude on \mathcal{L}_D is -3 in the linear regime of low applied voltages and approaches to -1 at high voltages. Qualitatively similar results are obtained for different δ and κH values. Despite the uncertainty in underlying impact of the applied voltage, asymptotic scaling arguments are straightforward:

$$\langle \tilde{E} \rangle_{\text{peak}} \propto \mathcal{L}_D^b, \quad (28)$$

where $b = -3$ and -1 for $\Phi_0 \sim 1$ and $\Phi_0 \gg 1$, respectively. It appears that by increasing the applied voltage, AREF becomes less sensitive to \mathcal{L}_D value, or in dimensional context, to the applied frequency and ion diffusivities. The underlying reasons for the precise scaling exponents, however, remain obscure.

D. Effect of ionic mobility mismatch (δ)

The ionic mobility mismatch ($\delta = D_-/D_+$) is perhaps the most intriguing parameter of the AREF effect. The AREF is plotted versus position for different δ values in Fig. 7(a). The effect of δ is non-monotonic: by increasing the ionic mobility mismatch from $\delta = 1$, the peak magnitude of AREF increases initially and then starts decaying. Hashemi Amrei et al. [57] showed that for $\delta < 1$, the AREF distribution would be the exact mirror of the displayed curves with respect to the zero line, i.e., it is antisymmetric. While δ has a considerable impact on the oscillatory behavior of AREF and its shape, it does not alter the peak location. A quantitative analysis of the peak magnitude for different conditions in which we change the \mathcal{L}_D and κH values reveals that the non-monotonic trend is robust (Fig. 7(b)).

The observed decay of the peak value can be explained via an asymptotic analysis of the problem. In the limit of $\delta \rightarrow \infty$ or $\delta \rightarrow 0$, one of the ions is extremely fast compared to the other nearly unmoving one. Under such conditions, the two-ion model (Fig. 1) predicts a zero time average electric field. In other words, the harmonic oscillations of the two ions are prerequisites of AREF effect: a single oscillating ion would not induce AREF as the time average of its sinusoidal oscillation is invariably zero.

The exact δ value at which $\langle \tilde{E} \rangle_{\text{peak}}$ reaches its maximum (δ_{max}) is however less straightforward. Based on the results shown in Fig. 7(b), δ_{max} is unresponsive to \mathcal{L}_D and κH values; the curves collapse under normalization. However, δ_{max} significantly depends on the applied potential. As depicted in Fig. 7(c), by increasing the applied potential, the summit of the curve shifts toward $\delta = 1$. This shift is quantitatively demonstrated in Fig. 7(d) for a range of $\Phi_0 = 0.1$ to $\Phi_0 = 100$. As shown in this figure, δ_{max} indefinitely decays from ≈ 5.25 toward $\delta = 1$ by increasing the applied voltage.

Physically, one way to understand this impact of the applied potential on the peak ionic mobility mismatch is as a measure of how far the ions displace during each cycle. At higher applied potentials, the ions are able to move further away from each other, and accordingly a higher fraction of the faster moving ions are able to ‘escape’ from the bulk into the double layers adjacent to each electrode. Since the existence of AREF depends on the mismatch between the two species of ions, the decrease in concentration of the speedier ions correspondingly decreases the magnitude of the AREF. At higher applied potentials, only smaller values of delta allow for

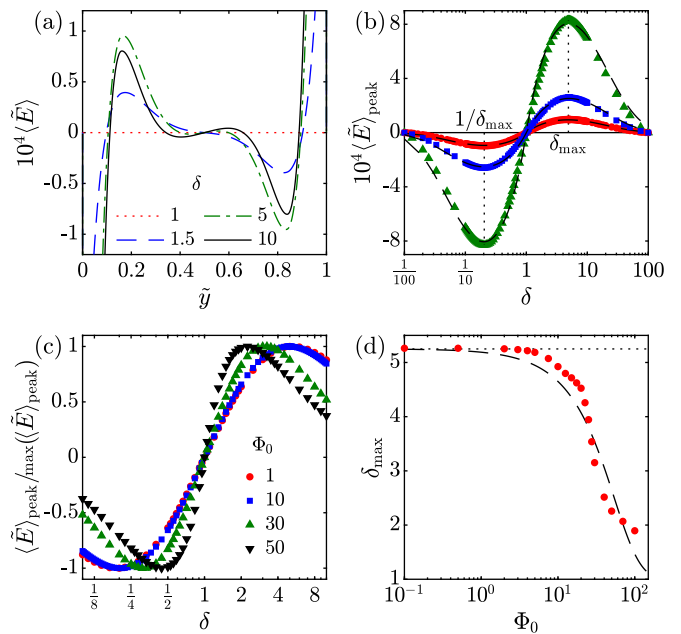


FIG. 7. Effect of δ on AREF behavior. (a) Spatial distribution of AREF for different δ values ($\Phi_0 = 10$, $\mathcal{L}_D = 0.2$, $\kappa H = 2600$). (b) Peak magnitude of AREF ($\langle \tilde{E} \rangle_{\text{peak}}$) versus δ for different conditions; markers: red circles, $\Phi_0 = 10$, $\mathcal{L}_D = 0.2$, $\kappa H = 2600$; blue squares, $\Phi_0 = 10$, $\mathcal{L}_D = 0.14$, $\kappa H = 2600$; green triangles, $\Phi_0 = 10$, $\mathcal{L}_D = 0.2$, $\kappa H = 822$; dashed black curves are empirical fits; cf. Sec. IV. (c) Normalized peak magnitude of AREF ($\langle \tilde{E} \rangle_{\text{peak}} / \max(\langle \tilde{E} \rangle_{\text{peak}})$) versus δ for different Φ_0 values ($\mathcal{L}_D = 0.2$, $\kappa H = 2600$). (d) δ_{max} versus Φ_0 ($\mathcal{L}_D = 0.2$, $\kappa H = 2600$); dashed black curve is an empirical fit; cf. Sec. IV.

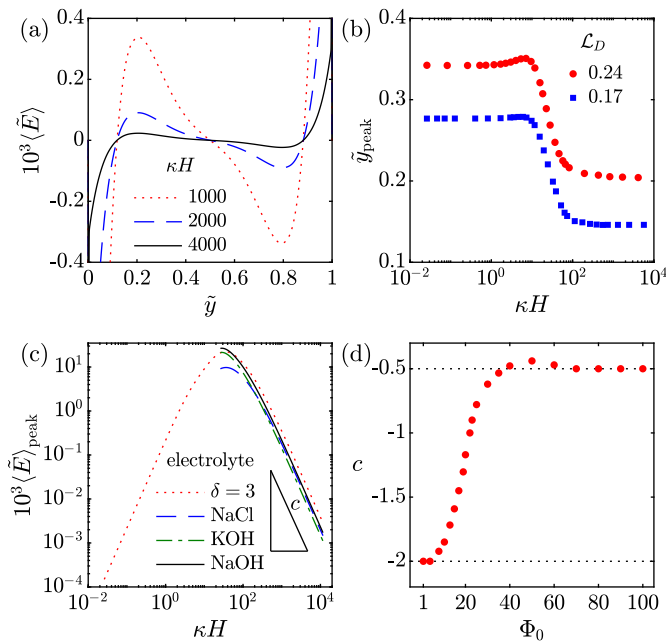


FIG. 8. Effect of κH on AREF behavior. (a) Spatial distribution of AREF for different κH values ($\Phi_0 = 10$, $\mathcal{L}_D = 0.24$, $\delta = 3$). (b) Peak location of AREF (\tilde{y}_{peak}) versus κH for two different values of \mathcal{L}_D ($\Phi_0 = 10$, $\delta = 3$). (c) Peak magnitude of AREF ($\langle \tilde{E} \rangle_{\text{peak}}$) versus κH for four different electrolytes of $\delta = 3$ ($\mathcal{L}_D = 0.24$), NaCl ($\delta = 1.52$, $\mathcal{L}_D = 0.23$), KOH ($\delta = 2.7$, $\mathcal{L}_D = 0.32$), and NaOH ($\delta = 3.95$, $\mathcal{L}_D = 0.29$) ($\Phi_0 = 10$). (d) Effect of Φ_0 on the power-law exponent c ($\mathcal{L}_D = 0.24$, $\delta = 3$).

the two ionic species to coexist at comparably high concentrations without one species escaping from the bulk, and δ_{max} decreases accordingly.

E. Effect of dimensionless Debye parameter (κH)

The dimensionless Debye parameter, which can be thought of as a measure of the ionic strength, also strongly affects the AREF behavior. As demonstrated in Fig. 8(a), upon changing the κH value, the general shape and peak location of the AREF distribution is conserved (similar to the effect of Φ_0). Recall that our focus is on the micron scale behavior of AREF; changing the κH value can alter the shape of AREF near the electrodes and within the Debye layer (not shown here). A more accurate analysis of the peak location however shows that the peak location depends only weakly on κH (Fig. 8(b)). A transition in the AREF behavior occurs at $10 \lesssim \kappa H \lesssim 100$ that abruptly changes the peak location. As an illustrative example, consider the case of $\mathcal{L}_D = 0.24$ in Fig. 8(b). For $\kappa H \gtrsim 100$, AREF peaks at $\tilde{y}_{\text{peak}} \approx 0.2$ (compare to curves in Fig. 8(a)). By decreasing the κH value, the peak location experiences a significant jump to ≈ 0.34 for $\kappa H \lesssim 10$. Still, for practical

conditions of electrokinetic systems where $H \sim 100 \mu\text{m}$ and $c_\infty > 10^{-5} \text{ M}$, $\kappa H \gg 100$ for aqueous electrolytes and the peak location remains unresponsive to changes in κH . So, in experiments such as particle height bifurcation [55, 56, 58], where the location of the peak is far more important than its magnitude (as long as it is large enough to result in electrophoretic levitation of colloidal particles), the results are not affected by κH .

Note that the transition in \tilde{y}_{peak} occurs near $\kappa H = 1$ to 10, i.e., in a range where the Debye layer is comparable in size to the electrodes spacing itself. Physically this suggests that the AREF spatial structure has two regimes: one in which the diffusive length scale interacts with the nature Debye length scale, and one in which they act more independently. Since $\kappa H \gg 1$ for many aqueous systems, it is the latter regime that is more relevant experimentally.

Figure 8(a) shows that how lower values of κH result in higher AREF magnitudes. This behavior is demonstrated in Fig. 8(c) for a wide range of κH values and four different electrolytes of $\delta = 3$ ($D_+ = 1 \times 10^{-9} \text{ m}^2/\text{s}$), NaCl, KOH, and NaOH. The results for all four electrolytes show that for practical electrolyte concentrations and electrode spacings, the AREF magnitude is inversely proportional to κH . The power-law exponent c however is a function of applied voltage (Fig. 8(d)). At low Φ_0 values, $c = -2$ and approaches -0.5 at higher applied voltages, which translates to c_∞^{-1} and $c_\infty^{-1/4}$ dependencies of the peak AREF magnitude on the electrolyte concentration, respectively. By decreasing κH to values where the Debye length is comparable to electrodes spacing, the peak magnitude starts dropping. This drop can be explained through the ionic strength; low κH can be a result of low electrolyte concentration and in asymptotically diluted solutions, the system is depleted of dissolved ions which drive the AREF effect.

F. Effect of ionic valences (z_+ & z_-)

The preceding sections focused on 1-1 electrolytes where $z_+ = |z_-| = 1$. We can introduce more asymmetry to the system by considering nonidentical valences (charge numbers) for the ions. Similar to the definition of $\delta = D_-/D_+$, we define $Z = |z_-/z_+|$ as the valence mismatch of the ions. Figures 9(a) & (b) present the AREF distribution for different combinations of z_+ and z_- values and two different δ values. For $\delta = 3$ (Fig. 9(a)), decreasing the Z value from 2 to 1/3 (dotted red curve to solid black curve) the peak magnitude of AREF decreases. This descending impact of the Z value on the AREF peak magnitude is more significant when δ is smaller (Fig. 9(b)), where changing the Z can even change the AREF direction. The results shown in Figs. 9(a) & (b) suggest that δ and Z affect AREF in the same qualitative way. In both cases of $\delta = 3$ and $\delta = 1.5$, decreasing the Z appears to reduce the impact of ionic mobility mismatch. However, if Z is small enough com-

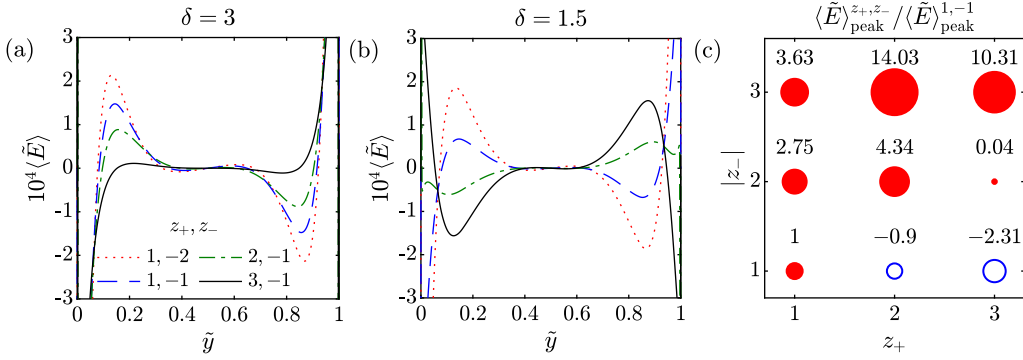


FIG. 9. Effect of the ion valences (z_+ and z_-) on the AREF behavior. (a & b) Spatial distribution of AREF for different z_+, z_- combinations and two values of δ . (c) Normalized peak magnitude of AREF ($\langle \tilde{E} \rangle_{\text{peak}}^{z_+, z_-} / \langle \tilde{E} \rangle_{\text{peak}}^{1, -1}$) for different z_+, z_- combinations and $\delta = 1.5$. Parameters: $\Phi_0 = 10$, $\mathcal{L}_D = 0.17$, $\kappa H = 2600$ for $z_+ = |z_-| = 1$ ($H = 25 \mu\text{m}$, 1 mM electrolyte).

pared to $1/\delta$ (equivalently, if Z is large enough compared to $1/\delta$ when $\delta < 1$), it can even qualitatively deform the AREF distribution (Fig. 9(b)). This behavior is analyzed more systematically in Fig. 9(c), which demonstrates the normalized magnitude and sign of the AREF peak for various combinations of z_+, z_- and a constant ionic mobility mismatch of $\delta = 1.5$. Note how changing the Z from 2 ($z_+, z_- = 1, -2$) to $1/2$ ($z_+, z_- = 2, -1$) changes the AREF direction. Also note that for the case of $z_+, z_- = 3, -2$ which yields $\delta Z = 1$, the AREF peak magnitude is very close to zero. Another interesting observation is that increasing the valences at a constant Z (possible only for $z-z$ electrolytes, assuming a maximum valence number of 3), appears to significantly increase the AREF peak magnitude (e.g., compare the cases of $z_+, z_- = 1, -1$ and $z_+, z_- = 3, -3$).

A rough approximation is that the product δZ determines the AREF direction. In the two ion model (Fig. 1), this idea can be incorporated easily by redefining the ionic mobility mismatch as $\delta = |D_- z_- / (D_+ z_+)|$. With the standard electrokinetic model however, the problem is more delicate. Although the electromigration term of the Nernst-Planck equation includes the product $D_i z_i$, the diffusivity and charge number appear separately in the diffusive contribution of the Nernst-Planck equation and free charge density term of the Poisson equation, respectively. In other words, the problem cannot be formulated by δZ as the sole term responsible for asymmetry.

IV. SCALING EXPRESSIONS

The preceding numerical results indicate that both the spatial structure and the magnitude of AREFs depend in a complicated fashion on the system parameters. In this section, we further elaborate the spatial structure, with an emphasis on identifying scaling expressions for where the AREF peaks in magnitude and how often it changes direction with respect to position. Furthermore, we present scaling expressions for the magnitude of the AREF in various asymptotic limits. For simplicity, the

analyses are performed for 1-1 electrolytes.

A. AREF length scale and structure

The dimensionless analysis indicates that \mathcal{L}_D is the only dimensionless parameter that affects the first peak location of AREF. This result is corroborated by a comparison of the numerically observed peak locations of AREF, \tilde{y}_{peak} plotted simply against the dimensionless diffusive length scale (Fig. 10). As shown in this figure, the diffusive length scale nicely predicts the peak location of AREF over a wide parameter space (more than 5000 numerical results). In other words, the peak loca-

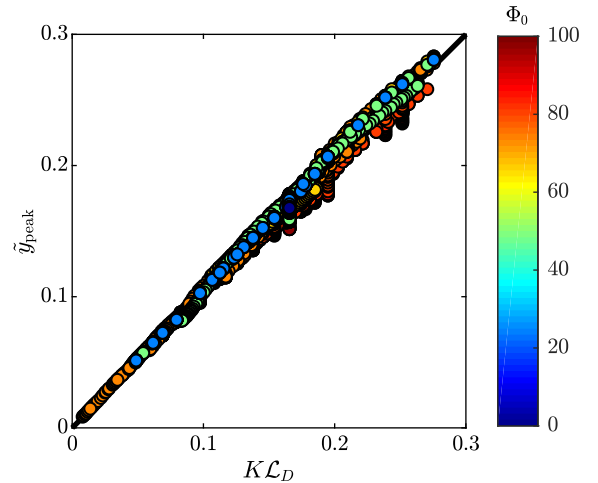


FIG. 10. Numerically observed peak location of AREF (\tilde{y}_{peak}) versus the predictions of the empirical formula $K\mathcal{L}_D = K\sqrt{D}/f/H$ for conditions that $\mathcal{L}_D < 1/3$. The correction coefficient is $K \approx 0.83$. Range of dimensional parameters (≈ 5000 data points): $0.1 \leq \phi_0 \leq 100 k_B T/e$, $1 \leq f \leq 30000 \text{ Hz}$, $2 \leq H \leq 100 \mu\text{m}$, $0.01 \leq \delta \leq 100$, $5 \times 10^{-10} \leq D_+ \leq 5 \times 10^{-9} \text{ m}^2/\text{s}$, $10^{-5} \leq c_\infty \leq 2 \times 10^{-2} \text{ M}$.

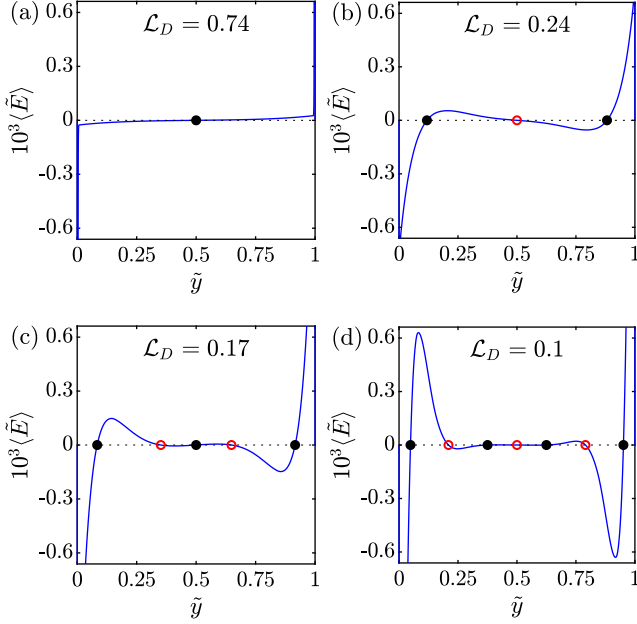


FIG. 11. Oscillatory behavior of AREF for different values of \mathcal{L}_D . Filled black and empty red circles are the points that AREF passes zero with positive and negative slopes, respectively. Parameters: $\Phi_0 = 10$, $\delta = 3$, $\kappa H = 2600$.

tion scales as

$$\tilde{y}_{\text{peak}} = K\mathcal{L}_D, \quad (29)$$

where the fitting prefactor $K \approx 0.83$ is obtained by linear regression. This result is significant since it provides an accurate and straightforward prediction for the AREF peak location for any condition (at least, over the wide range of values tested here). This finding also justifies $\hat{D} = \sqrt{D_+ D_-}$ as the correct characteristic diffusivity governing the AREF behavior.

Another important point to consider is the spatially oscillatory behavior of AREF (Fig. 11), which is controlled by the dimensionless parameters \mathcal{L}_D and δ ; as demonstrated in Secs. III B & III E, Φ_0 and κH do not affect the spatial structure of the AREF. For large values of \mathcal{L}_D , AREF passes zero only once with no peak outside the Debye layer (Fig. 11(a), $\mathcal{L}_D = 0.74$). Upon decreasing \mathcal{L}_D (or equivalently, increasing the frequency), first a peak appears with AREF passing zero three times (Fig. 11(b), $\mathcal{L}_D = 0.24$). Further decreasing the \mathcal{L}_D value results in 5 and then 7 zeros (Figs. 11(c) & (d)). In other words, when \mathcal{L}_D decreases, there is more space for AREF to oscillate and change sign. Note that AREF is always zero at the midplane. The oscillatory behavior of the AREF can be further analyzed by the bifurcation diagram demonstrated in Fig. 12(a). Consistent with the results provided in Fig. 11, at high \mathcal{L}_D values, there is only one zero which occurs at the midplane. As \mathcal{L}_D decreases, pitchfork bifurcations [65] occur at the midplane. After each bifurcation, two more zeros are added to the system

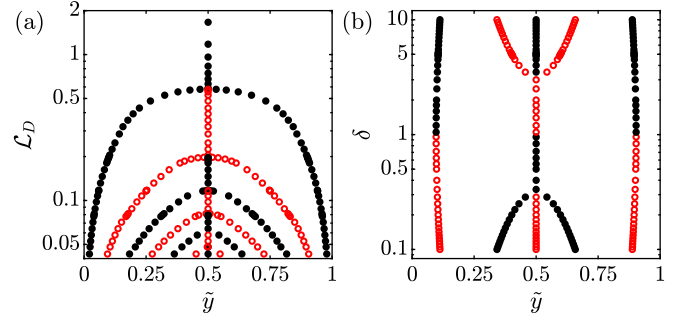


FIG. 12. Bifurcation diagrams of AREF for \mathcal{L}_D (a) and δ (b) as varying parameters. Filled black and empty red circles are the points that AREF passes zero with positive and negative slopes, respectively. Parameters: $\Phi_0 = 10$, $\mathcal{L}_D = 0.2$ (b), $\delta = 3$ (a), $\kappa H = 2600$.

while the slope of the AREF at the midplane switches.

Despite the fact that \mathcal{L}_D determines the peak location of AREF, it is not the only dimensionless parameter controlling the number of zeros. Fig. 7(a) shows that, for constant \mathcal{L}_D , the first AREF peak is independent of the precise δ value. However, the δ value can shift and deform the smaller peaks of the distribution and consequently the overall number of zeros (cf. the cases of $\delta = 1.5$ and 10 in Fig. 7(a)). This behavior is plotted quantitatively in the bifurcation diagram in Fig. 12(b), showing the number of zeros for different δ values. For δ values close to 1, the AREF passes zero three times; by increasing/decreasing the δ value from 1 pitchfork bifurcations happen at the midplane.

B. AREF magnitude scaling

Based on the results presented in Sec. III, $\langle \tilde{E} \rangle_{\text{peak}} \propto \Phi_0^a$, $\langle \tilde{E} \rangle_{\text{peak}} \propto \mathcal{L}_D^b$, and $\langle \tilde{E} \rangle_{\text{peak}} \propto (\kappa H)^c$. Here the power a increases non-monotonically from 1 in the linear regime ($\Phi_0 \sim 1$) to a maximum in the nonlinear regime, before decaying to a small constant value at very high applied voltages (cf. Fig. 5(c)). The powers b and c are -3 and -2 for $\Phi_0 \sim 1$ and approach to -1 and -0.5 for $\Phi_0 \gg 1$, respectively.

The effect of δ is more complicated. The non-monotonic behavior demonstrated in Fig. 7(b) may be approximated by the empirical fits

$$\langle \tilde{E} \rangle_{\text{peak}} = c_1 \alpha \exp(-c_2 |\alpha|), \quad (30)$$

where

$$\alpha = \sqrt{\delta} - 1/\sqrt{\delta} = (D_- - D_+)/\hat{D}. \quad (31)$$

Knowing δ_{max} , one can easily find the coefficient c_2 by differentiation of the fitting curve formula as $c_2 = 1/\alpha_{\text{max}}$, where

$$\alpha_{\text{max}} = \sqrt{\delta_{\text{max}}} - 1/\sqrt{\delta_{\text{max}}}. \quad (32)$$

Finally we get

$$\langle \tilde{E} \rangle_{\text{peak}} \propto \alpha \exp(-|\alpha|/\alpha_{\text{max}}), \quad (33)$$

where α_{max} is a function of the applied voltage (Fig. 7(d)). Unlike b and c , δ_{max} does not appear to approach a certain value at high voltages. Hence, to provide scaling expressions at high voltages, we use an empirical formula to fit the δ_{max} vs Φ_0 data. The fitting curve in Fig. 7(d) is a sigmoid function

$$\delta_{\text{max}} = k_1 - k_2 \frac{e^{k_3 \Phi_0}}{1 + e^{k_3 \Phi_0}}. \quad (34)$$

We can find the coefficients k_1 and k_2 enforcing the conditions $\delta_{\text{max}} \rightarrow 5.25$ as $\Phi_0 \rightarrow 0$ and $\delta_{\text{max}} \rightarrow \delta_{\infty}$ as $\Phi_0 \rightarrow \infty$. The final value of $\delta_{\text{max}} = \delta_{\infty}$ is unclear, due to the lack of numerical results at extremely high voltages. However, we can make a reasonable assumption: note that δ_{max} indefinitely gets closer to 1 by increasing the Φ_0 ; considering this descending trend, along with the fact that it is already below 2 for $\Phi_0 = 100$, we hypothesize that δ_{max} eventually approaches 1. Using these conditions, we find the coefficients $k_1 = 9.5$ and $k_2 = 8.5$. The last coefficient k_3 is found by fitting as $k_3 \approx 0.03$. Of course a better fitting formula could be employed but at the expense of simplicity.

A possible scaling of the AREF peak magnitude can then be obtained by multiplication of all scaling arguments as

$$\langle \tilde{E} \rangle_{\text{peak}} \propto \Phi_0^a \mathcal{L}_D^b (\kappa H)^c \gamma, \quad (35)$$

where $\gamma = \alpha \exp(-|\alpha|/\alpha_{\text{max}})$ with $\alpha_{\text{max}} = \sqrt{\delta_{\text{max}}} - 1/\sqrt{\delta_{\text{max}}}$ and δ_{max} given by the empirical formula in Eq. 34.

Although the complicated impact of Φ_0 obscures any generalized scaling analysis, asymptotic expressions can be obtained. We consider two different regimes of applied voltages as low-intermediate ($0 < \Phi_0 \leq 20$) and intermediate-high ($20 \leq \Phi_0 \leq 100$). The underlying reason of this division is the variations of b , c , and δ_{max} with Φ_0 . The applied voltage of $\Phi_0 = 20$ is approximately at the middle of transition from low to high applied voltages regimes (cf. Figs 6(d), 7(d), & 8(d)). Besides, the summit of power a in Fig. 5(c), occurs around $\Phi_0 \approx 20$, regardless of the system properties.

Substituting $a = 1, b = -3, c = -2$ gives the simplified scaling argument at low-intermediate applied voltages:

$$\Phi_0 \leq 20: \quad \langle \tilde{E} \rangle_{\text{peak}} \approx K \frac{\Phi_0 \gamma}{\mathcal{L}_D^3 (\kappa H)^2}, \quad (36)$$

where the coefficient K is obtained by fitting as $K \approx 0.19$. Figure 13(a) shows a comparison between the numerically observed peak magnitude of AREF and predictions of Eq. 36. Note that Eq. 36 captures the AREF peak magnitude extremely well for $\Phi_0 < 5$ (blue points in Fig. 13(a)). For intermediate voltages, it is only the power a that is increasing from 1, while the data points

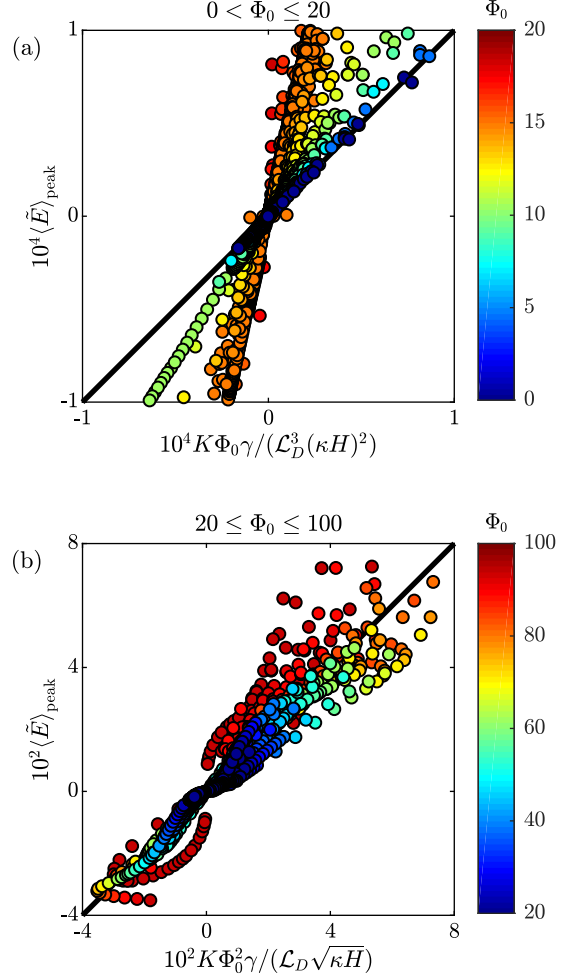


FIG. 13. Numerically observed peak magnitude of AREF ($\langle \tilde{E} \rangle_{\text{peak}}$) versus the predictions of the empirical formula ($\langle \tilde{E} \rangle_{\text{peak}} \approx \Phi_0^a \mathcal{L}_D^b \gamma (\kappa H)^c$ for conditions that $\mathcal{L}_D < 1/3$). (a) Low to moderate voltages ($0 < \Phi_0 \leq 20$): fitting is performed using low voltage data ($\Phi_0 < 5, K \approx 0.19$). (b) Moderate to high voltages ($20 \leq \Phi_0 \leq 100$): fitting is performed using all data points ($K \approx 2 \times 10^{-4}$). Range of dimensional parameters (≈ 5000 data points): $0.1 \leq \phi_0 \leq 100$ $k_B T/e$, $1 \leq f \leq 30000$ Hz, $2 \leq H \leq 100$ μm , $0.01 \leq \delta \leq 100$, $5 \times 10^{-10} \leq D_+ \leq 5 \times 10^{-9}$ m^2/s , $10^{-5} \leq c_\infty \leq 2 \times 10^{-2}$ M.

are still nicely linear. Recall that the power a increases monotonically from 1 at low-intermediate values of Φ_0 (cf. Fig. 5(c)).

Similarly, we can insert $b = -1, c = -0.5$ to find the scaling expression at intermediate-high applied voltages. Since this range of applied voltage ($0.5 \leq \phi_0 \leq 2.5$ volts, or peak-to-peak applied voltages of 1–5 volts) is frequently used in electrokinetic experiments we prefer to fit the data using all results. So instead of substituting an a value below 1 (cf. Fig. 5(c) at very high Φ_0 values), we heuristically find a value that collapse all data points. Our analysis shows that an average of summit and final a values ($a \approx 2$) is a good choice. Hence, the scaling

expression at intermediate-high applied voltages can be written as

$$\Phi_0 \geq 20: \quad \langle \tilde{E} \rangle_{\text{peak}} \approx K \frac{\Phi_0^2 \gamma}{\mathcal{L}_D \sqrt{\kappa H}}, \quad (37)$$

with $K \approx 2.1 \times 10^{-4}$ obtained from linear regression. The corresponding comparison provided in Fig. 13(b) shows that the prediction of Eq. 37 is in the right neighborhood, (R-square ≈ 0.9), differing by at most a factor of 2 over the entire range of parameters tested. This scaling estimate should help in interpretation of experimental results involving AREFs.

V. CONCLUSIONS

In summary, we have comprehensively investigated the AREF phenomenon reported recently by Hashemi Amrei et al. [57]. The effects of various parameters including the applied voltage and frequency, ionic mobility mismatch, mobilities of the dissolved ions, ionic strength, electrodes spacing, and valences of the ions on the spatial structure and magnitude of the AREF were analyzed in detail.

Dimensionless analysis of the problem shows that the diffusive length scale ℓ_D , with $\sqrt{D_+ D_-}$ as the characteristic diffusivity, can accurately predict the peak location of the AREF in a wide spectrum of system properties. The AREF magnitude, in contrast, is found to be more complicated, mainly due to the confounding nonlinear impacts of the applied voltage. Regardless of the system properties, at low applied voltages the peak magnitude of AREF varies as the square of the applied potential. No universal correlation is found for larger voltages, i.e., no simple power law behavior is observed. This peculiar influence of the applied potential complicates the analy-

ses of the other dimensionless parameters. Our observations indicate that the AREF peak magnitude decreases by increasing the diffusive length scale (i.e., decreasing the frequency), with the rate of decrease sensitive to the applied voltage. The analysis indicates that the AREF magnitude becomes less sensitive to \mathcal{L}_D at higher voltages, for reasons that remain obscure. The ionic mobility mismatch has a pronounced non-monotonic impact on the AREF magnitude, increasing from zero at $\delta = 1$ to a maximum at a voltage-dependent δ_{max} . Physically, this result stems from the necessity for the two ionic species to oscillate asymmetrically; in the limit where $\delta = 1$ there is no asymmetry (and hence no AREF), and as $\delta \rightarrow \infty$ effectively only one ion oscillates appreciably, again yielding no AREF. Finally, we find that for most aqueous systems the AREF magnitude decreases inversely with the ionic concentration at low applied voltages, or as the inverse one fourth power ($c_\infty^{-1/4}$) at higher voltages. Combining the obtained results from the numerical analyses for the various parameters yields simplified approximate scaling arguments that should assist researchers in interpretation and control of experiments.

While the above-mentioned results were obtained for univalent electrolytes, we also demonstrated that introducing asymmetry through nonidentical ion valences is as important as the ionic mobility mismatch. Furthermore, the results presented here are limited to situations where electrochemical, Stern layer, and convective contributions to the flux are negligible. These more complicated effects are deferred to future studies.

ACKNOWLEDGMENTS

This material is based upon work partially supported by the National Science Foundation under Grant No. DMS-1664679.

-
- [1] A. Ramos, H. Morgan, N. G. Green, and A. Castellanos, *J. Phys. D: Appl. Phys.* **31**, 2338 (1998).
 - [2] A. Ramos, H. Morgan, N. G. Green, and A. Castellanos, *J. Colloid Interface Sci.* **217**, 420 (1999).
 - [3] A. Ajdari, *Phys. Rev. E* **61**, R45(R) (2000).
 - [4] V. Studer, A. Pepin, Y. Chen, and A. Ajdari, *Analyst* **129**, 944 (2004).
 - [5] N. I. Gamayunov, V. A. Murtsovkin, and A. S. Dukhin, *Colloid J.* **48**, 197 (1986).
 - [6] A. S. Dukhin and V. A. Murtsovkin, *Colloid J.* **48**, 203 (1986).
 - [7] S. S. Dukhin, *Adv. Colloid Interface Sci.* **35**, 173 (1991).
 - [8] V. A. Murtsovkin, *Colloid J.* **58**, 341 (1996).
 - [9] M. Z. Bazant and T. M. Squires, *Phys. Rev. Lett.* **92**, 066101 (2004).
 - [10] T. M. Squires and M. Z. Bazant, *J. Fluid Mech.* **509**, 217 (2004).
 - [11] S. Gangwal, O. J. Cayre, M. Z. Bazant, and O. D. Velev, *Phys. Rev. Lett.* **100**, 058302 (2008).
 - [12] M. Z. Bazant, M. S. Kilic, B. D. Storey, and A. Ajdari, *Adv. Colloid Interface Sci.* **152**, 48 (2009).
 - [13] T. M. Squires, *Lab Chip* **9**, 2477 (2009).
 - [14] S. M. Davidson, M. B. Andersen, and A. Mani, *Phys. Rev. Lett.* **112**, 128302 (2014).
 - [15] M. Trau, D. A. Saville, and I. Aksay, *Science* **272**, 706 (1996).
 - [16] M. Trau, D. A. Saville, and I. A. Aksay, *Langmuir* **13**, 6375 (1997).
 - [17] D. C. Prieve, P. J. Sides, and C. L. Wirth, *Curr. Opin. Colloid Interface Sci.* **15**, 160 (2010).
 - [18] F. Ma, S. Wang, L. Smith, and N. Wu, *Adv. Funct. Mater.* **22**, 4334 (2012).
 - [19] C. S. Dutcher, T. J. Woehl, N. H. Talken, and W. D. Ristenpart, *Phys. Rev. Lett.* **111**, 128302 (2013).
 - [20] X. Yang and N. Wu, *Langmuir* **34**, 952 (2018).
 - [21] H. Zhou, L. R. White, and R. D. Tilton, *J. Colloid In-*

- terface Sci. **285**, 179 (2005).
- [22] J. Voldman, *Annu. Rev. Biomed. Eng.* **8**, 425 (2006).
- [23] T. Z. Jubery, S. K. Srivastava, and P. Dutta, *Electrophoresis* **35**, 691 (2014).
- [24] Z. Zheng, B. Jing, M. Sorci, G. Belfort, and Y. Zhu, *Biomicrofluidics* **9**, 044123 (2015).
- [25] A. D. Hollingsworth and D. A. Saville, *J. Colloid Interface Sci.* **257**, 65 (2003).
- [26] C. Grosse and A. V. Delgado, *Curr. Opin. Colloid Interface Sci.* **15**, 145 (2010).
- [27] P. J. Beltramo, R. Roa, F. Carrique, and E. M. Furst, *J. Colloid Interface Sci.* **408**, 54 (2013).
- [28] K. Mukherjee, G. Schwaab, and M. Havenith, *Phys. Chem. Chem. Phys.* **20**, 29306 (2018).
- [29] A. S. Bandarenka, *Analyst* **138**, 5540 (2013).
- [30] H. Wang, A. Thiele, and L. Pilon, *J. Phys. Chem. C* **117**, 18286 (2013).
- [31] D. Koster, G. Du, A. Battistel, and F. L. Mantia, *Electrochim. Acta* **246**, 553 (2017).
- [32] R. Hidalgo-Alvarez, A. Martln, A. Fernandez, D. Bastos, F. Martinez, and F. J. de las Nieves, *Adv. Colloid Interface Sci.* **67**, 1 (1996).
- [33] A. V. Delgado, F. Gonzalez-Caballero, R. J. Hunter, L. K. Koopal, and J. Lyklema, *Adv. Colloid Interface Sci.* **309**, 194 (2007).
- [34] R. Puset, S. Gourdin-Bertin, E. Dubois, J. Chevalet, G. Meriguet, O. Bernard, V. Dahirel, M. Jardatab, and D. Jacobc, *Phys. Chem. Chem. Phys.* **17**, 11779 (2015).
- [35] P. R. C. Gascoyne and J. Vykoukal, *Electrophoresis* **23**, 1973 (2002).
- [36] R. Pethig, *Biomicrofluidics* **4**, 022811 (2010).
- [37] H. Zhao, *Electrophoresis* **32**, 2232 (2011).
- [38] A. Koklu, A. C. Sabuncu, and A. Beskok, *Electrophoresis* **38**, 1458 (2017).
- [39] H. Frusawa, *Nanoscale Res. Lett.* **13**, 169 (2018).
- [40] J. Catalano, H. V. M. Hamelers, A. Bentien, and P. M. Biesheuvel, *J. Phys. Condens. Matter* **28**, 324001 (2016).
- [41] J. Catalano and P. M. Biesheuvel, *Europhys. Lett.* **123**, 58006 (2018).
- [42] W. B. Russel, D. A. Saville, and W. R. Schowalter, *Colloidal Dispersions*, 1st ed. (Cambridge University Press, 1989).
- [43] E. H. B. Delacey and L. R. White, *J. Chem. Soc., Faraday Trans. 2* **77**, 2007 (1981).
- [44] E. J. Hinch and J. D. Sherwood, *J. Chem. Soc., Faraday Trans. 2* **80**, 535 (1984).
- [45] C. S. Mangelsdorf and L. R. White, *J. Chem. Soc., Faraday Trans.* **93**, 3145 (1997).
- [46] M. Z. Bazant, K. Thornton, and A. Ajdari, *Phys. Rev. E* **70**, 021506 (2004).
- [47] L. H. Olesen, M. Z. Bazant, and H. Bruus, *Phys. Rev. E* **82**, 011501 (2010).
- [48] O. Schnitzer and E. Yariv, *Phys. Rev. E* **89**, 032302 (2014).
- [49] R. F. Stout and A. S. Khair, *Phys. Rev. E* **92**, 032305 (2015).
- [50] J. Kim, J. L. Anderson, S. Garoff, and P. J. Sides, *Langmuir* **18**, 5387 (2002).
- [51] J. D. Hoggard, P. J. Sides, and D. C. Prieve, *Langmuir* **23**, 6983 (2007).
- [52] J. D. Hoggard, P. J. Sides, and D. C. Prieve, *Langmuir* **24**, 2977 (2008).
- [53] C. L. Wirth, P. J. Sides, and D. C. Prieve, *Phys. Review. E* **87**, 032302 (2013).
- [54] T. J. Woehl, K. L. Heatley, C. S. Dutcher, N. H. Talken, and W. D. Ristenpart, *Langmuir* **30**, 4887 (2014).
- [55] T. J. Woehl, B. J. Chen, K. L. Heatley, N. H. Talken, S. C. Bukosky, C. S. Dutcher, and W. D. Ristenpart, *Phys. Rev. X* **5**, 011023 (2015).
- [56] S. C. Bukosky and W. D. Ristenpart, *Langmuir* **31**, 9742 (2015).
- [57] S. M. H. Hashemi Amrei, S. C. Bukosky, S. P. Rader, W. D. Ristenpart, and G. H. Miller, *Phys. Rev. Lett.* **121**, 185504 (2018).
- [58] S. C. Bukosky, S. M. H. Hashemi Amrei, S. P. Rader, J. Mora, G. H. Miller, and W. D. Ristenpart, Submitted.
- [59] R. W. O'Brien and L. R. White, *J. Chem. Soc., Faraday Trans. 2* **74**, 1607 (1978).
- [60] C. Hughes, L. Yeh, and S. Qian, *J. Phys. Chem. C* **117**, 9322 (2013).
- [61] W. L. Briggs, V. E. Henson, and S. F. McCormick, *A Multigrid Tutorial*, 2nd ed. (SIAM, 2000).
- [62] G. Miller, *Numerical Analysis for Engineers and Scientists* (Cambridge University Press, 2014).
- [63] D. F. Martin and K. L. Cartwright, *Solving Poisson's Equation Using Adaptive Mesh Refinement*, Technical Report UCB/ERL M96/66 (UC Berkeley, 1996).
- [64] M. Z. Bazant, M. S. Kilic, B. D. Storey, and A. Ajdari, *New J. Phys.* **11**, 075016 (2009).
- [65] S. H. Strogatz, *Nonlinear Dynamics and Chaos* (Addison-Wesley Publishing Company, 1994).